Research on the Effect of Geometric Parameters of a Six-Way Junction Microchannel on the Formation of a Double Emulsion Droplet

B. S. Xie, F. Jiang[†], H. J. Lin, M. C. Zhang, J. Shen and J. H. Xiang

School of Mechanical and Electrical Engineering, Guangzhou University, Guangzhou 510006, China

†*Corresponding Author Email: jiangfan2008@gzhu.edu.cn*

ABSTRACT

As a typical microdroplet, double emulsion droplet, has received much attention and been widely used in recent years. For a simplified double-cross-shaped microchannel, the process of preparing double emulsion droplets is numerically simulated in this paper. The mechanism of droplet forming was analyzed, and the effects of the angles of the inner-, middle-, and outer-phase channels of the microchip, length of the focusing hole, and expansion angle on the process and quality of the double emulsion droplet formation were investigated. The variation in angles between each inlet channel affects the droplet area; the change in expansion angle affects the flow pattern of droplets; the change in each geometric parameter affects the monodispersity of droplets. The droplet area is fitted to the microchannel geometric parameters and the functional expressions that represent their relationship are derived. The work in this paper provides a reference for the practical production and research of double emulsion droplets.

NOMENCLATURE

b_1	volume fraction of inner phase	S_{min}	minimum area of droplets
b_2	volume fraction of middle phase	S_i	area of inner droplets
b_3	volume fraction of outer phase	S_o	area of outer droplets
C_a	capillary number	SD	standard deviation of data
$C.V.$	coefficient of variation	t	time
CV_i	coefficient of variation for inner droplet areas	$\vec{v}$	velocity vector
CV_o	coefficient of variation for outer droplet areas	w_1	width of inner phase channel
		w_2	width of middle phase channel
F	interfacial tension and gravity	W_e	Weber number
F_L	linear momentum force	α_1	angle between inner- and middle-phase channel
F_S	Stokes-like force		
F_σ	interfacial tension	α_2	angle between middle- and outer-phase channel
l	characteristic length		
L	length of focusing hole	α_3	expansion angle
L_1	distance between droplet breaking point and microchip intersection	ρ	density
		ρ_d	density of double emulsion droplet
L_2	distance between droplet breaking point and microchip intersection	ρ_1	density of inner phase
		ρ_2	density of middle phase
MN	mean of data	ρ_3	density of outer phase
P	pressure	μ	dynamic viscosity
Q_1	flow rate of inner phase	μ_d	viscosity of double emulsion droplet
Q_2	flow rate of middle phase	μ_1	viscosity of inner phase
Q_3	flow rate of outer phase	μ_2	viscosity of middle phase
S	maximum area variation ratio	μ_3	viscosity of outer phase
S_1	maximum area variation ratio of	σ	interfacial tension between two

	inner droplets		phases
S_2	maximum area variation ratio of outer droplets	σ_{12}	interfacial tension between inner and middle phase
S_{max}	maximum area of droplets	σ_{23}	interfacial tension between middle and outer phase

1. INTRODUCTION

Microfluidics is a technology that handles microfluidics (Shao *et al.* 2021). As an essential branch of microfluidics, droplet microfluidics mainly uses the interaction of microfluidic shearing force, viscous force, and interfacial tension to split continuous fluid into dispersed droplets (Han and Chen 2021). One of the extremely promising directions in droplet microfluidics is the preparation of double emulsion droplets using this technique. These techniques have been widely used in various fields, such as self-healing materials (Souza and Al-Tabbaa 2018; Zhang *et al*. 2018), electrochemical biosensors (Schmidt-Speicher and Länge 2021; Xing *et al*. 2021; Muhsin *et al*. 2022), food processing and safety (He *et al*. 2020; Su *et al*. 2021), biomedicine (Illath *et al*. 2021; Shi *et al*. 2021; Ko *et al*. 2022), and chemically enhanced oil recovery (Fani *et al*. 2022). Therefore, it is of great practical production significance to investigate the forming mechanism and process of double emulsion droplets.

Nabavi *et al*. (2015) developed a three-phase axisymmetric numerical model and conducted numerical simulations in ANSYS Fluent fluid analysis software to investigate the effects of physical properties (such as the flow rate, fluid interfacial tension, viscosity, and density of each phase) and geometric parameters (such as distance between the fluid inlet and outlet) on the forming droplet size, pattern, and production rate. Stauffer *et al*. (2019) modified the wetting properties of the microchip to generate microdroplets with controlled size and shell thickness. Lian *et al*. (2019) investigated the effect of microfluidic interfacial tension on the stepwise emulsification of microdroplets by numerical simulations using ANSYS Fluent. Zhao-Miao *et al*. (2018) used a combination of experimental and numerical simulations to investigate the effects of the flow rate of three phases on the forming pattern, size, and frequency of double emulsion droplets. Liu *et al*. (2021) investigated the effect of the viscosity of the dispersed phase on the microfluidic flow state transition and droplet size in a flow-focusing device. Liu *et al*. (2018) investigated the effect of expansion angle at the intersection in T-shaped microchannels on droplet formation. Hidema *et al*. (2021) investigated droplet formation in a microchip with a triangular expansion angle. Sartipzadeh *et al*. (2020) investigated the effect of the geometry of a cross-shaped microchannel on droplet formation. Many scholars have investigated the effects of microfluidic flow properties and geometrical parameters of microchannels on microdroplet formation.

Deshpande *et al*. (2016) proposed a simplified double-cross-shaped microchannel with a six-way junction in their investigation of microdroplet preparation. The microchannel has a simple structure and is suitable for preparing microdroplets, such as double emulsion droplet, since it is easy to control droplet formation with proper adjustment of the structure. Other scholars have also prepared microdroplets using microchannels with this structure (Deshpande and Dekker 2018; Schaich *et al*. 2020; Vaezi *et al*. 2020; Tivony *et al*. 2021).

Microchips such as double-cross and double-T shaped ones are multilayered in series and have high manufacturing costs, while the simplified double-cross structure of the six-way junction shape in this paper is beneficial to reduce the chip area. The effect of fluid properties on the double emulsion droplet formation has been investigated using chips of this structure (Tan *et al* 2020). However, the effect of the microchip geometry on the droplet formation has been less investigated. In this paper, numerical simulations are used to investigate the effect of the geometrical parameters of microchannels on droplet formation for this simplified double-cross-shaped microchannel. In this paper, the forming area and monodispersity of double emulsion droplets are investigated by varying the angles between the inner and middle phase, middle- and outer-phase channels, width ratio between inner- and middle-phase channels, and expansion angle of the microchip. To make the statistical results with less error, each time the geometrical structure parameters are changed, 5 stably forming double emulsion droplets are selected to count the average value of their forming area size. These average values are used for comparison under different geometric structure parameters.

2. CONTROL EQUATIONS, DIMENSIONLESS PARAMETERS, AND EVALUATION PARAMETERS

The volume of fluid method (VOF) is often applied to multiphase flow calculation problems (Jiang *et al*. 2019) and is used for numerical simulations in this paper. The basic theoretical basis for numerical simulation is the basic control equations of fluid motion, such as the continuity equation and conservation of momentum equation. Dimensionless parameters such as the capillary number and Weber number are often used to analyze the force on droplets (Nabavi *et al*. 2015). The coefficient of variation is often used to measure the degree of data dispersion (Deshpande *et al*. 2016). In this paper, the concept of maximum area variation rate is introduced to measure the relative wall thickness of the droplet.

2.1 Volume of Fluid Method (VOF)

When VOF is used to characterize the motion of each phase interface, the equations for the density and

viscosity of a double emulsion droplet are shown in Eqs. (1) and (2).

$$\rho_d = b_1\rho_1 + b_2\rho_2 + b_3\rho_3 \tag{1}$$

$$\mu_d = b_1\mu_1 + b_2\mu_2 + b_3\mu_3 \tag{2}$$

where ρ_d is the density of a droplet; b_1, b_2 and b_3, are the volume fractions of the three phases; ρ_1, ρ_2, and ρ_3 are the densities of the three phases; μ_d is the viscosity of a droplet; μ_1, μ_2, and μ_3 are the viscosities of the three phases.

2.2 Continuity Equation

The continuity equation is shown in Eq. (3).

$$\frac{\partial \rho}{\partial t} + \nabla \cdot (\rho \vec{v}) = 0 \tag{3}$$

where ρ is the density, t is the time, and $\vec{v}$ is the velocity vector.

2.3 Conservation of Momentum Equation

The fluid momentum conservation equation is shown in Eq. (4).

$$\frac{\partial \vec{v}}{\partial t} + \nabla \cdot (\vec{v}\vec{v}) = -\frac{1}{\rho}\nabla P + \nabla \cdot \frac{\mu}{\rho}[\nabla \vec{v} + \nabla(\vec{v})^{\mathrm{T}}] + F \tag{4}$$

where P is the pressure, μ is the dynamic viscosity, and F includes the interfacial tension and gravity.

2.4 Dimensionless Parameters

The capillary number C_a reflects the effect of the interfacial tension on the fluid flow, which is proportional to the ratio of the viscous force and interfacial tension. It is calculated by Eq. (5).

$$C_a = \frac{\mu \vec{v}}{\sigma} \tag{5}$$

where σ is the interfacial tension.

Weber number W_e is often used to analyze the fluid motion when there is a cross interface between different fluids. A smaller Weber number corresponds to more important interfacial tension. It is calculated as shown in Eq. (6).

$$W_e = \frac{\rho \vec{v}^2 l}{\sigma} \tag{6}$$

where l is the characteristic length.

2.5 Evaluation Parameters

The degree of data dispersion is inferred by calculating the coefficient of variation (*C.V.*); a smaller coefficient of variation corresponds to less discrete data, and it is calculated by Eq. (7).

$$C.V. = \frac{SD}{MN} \tag{7}$$

where *SD* is the standard deviation of the data, and *MN* is the mean of the data.

For the convenience of presentation, the coefficients of variation of the inner and outer droplets of the double emulsion droplets are subsequently expressed using CV_i and CV_o, respectively.

2.6 Maximum Area Variation Rate

The maximum area variation ratio *S* is defined as the ratio of the maximum to the minimum area of inner or outer droplets. A larger ratio corresponds to a greater relative wall thickness of the droplet. It is calculated by Eq. (8).

$$S = \frac{S_{max}}{S_{min}} \tag{8}$$

where S_{max} is the maximum area of droplets and S_{min} is the minimum area of droplets.

The maximum area variation ratios of the inner and outer droplets of the double emulsion droplet are subsequently expressed using S_1 and S_2, respectively.

3. NUMERICAL SIMULATION MODEL

3.1 Geometric Model and Physical Properties

To simplify the calculation, the object of numerical simulation is a two-dimensional microchip. The initial dimensions (unit: μm) of the microchip model are shown in Fig. 1. (a) The coordinate system, boundary names, and variable structural parameters are shown in Fig. 1. (b) The initial widths of the inlets of three phases are 160 μm, 60 μm, and 200 μm. The double emulsion droplet technology is widely used in the food industry and other industries (Kanouni et al., 2002; Sapei et al., 2012), and the densities of the fluids set for the numerical simulations in this paper are similar to those of pure water and cooking oil. The densities of the fluids selected for the numerical simulations are all 1000. For the fluid flow properties, subscripts 1, 2, and 3 are used in this paper to represent the inner, middle, and outer phases, respectively.

The chip designed in this paper belongs to the flow-focusing structure. According to existing studies, the main factors that affect droplet formation are the angles and width ratios of the inlet channels and the expansion angle. In this paper, we focused on the angles (the angle between inner- and middle-phase channels α_1, the angle between middle- and outer-phase channels α_2), the width ratio between the inner- and middle-phase channels w_1/w_2, and the expansion angle (the length of focusing hole *L* and the expansion angle α_3) to investigate the effects of these microchannel geometrical parameters on the droplet formation.

(a)   (b)
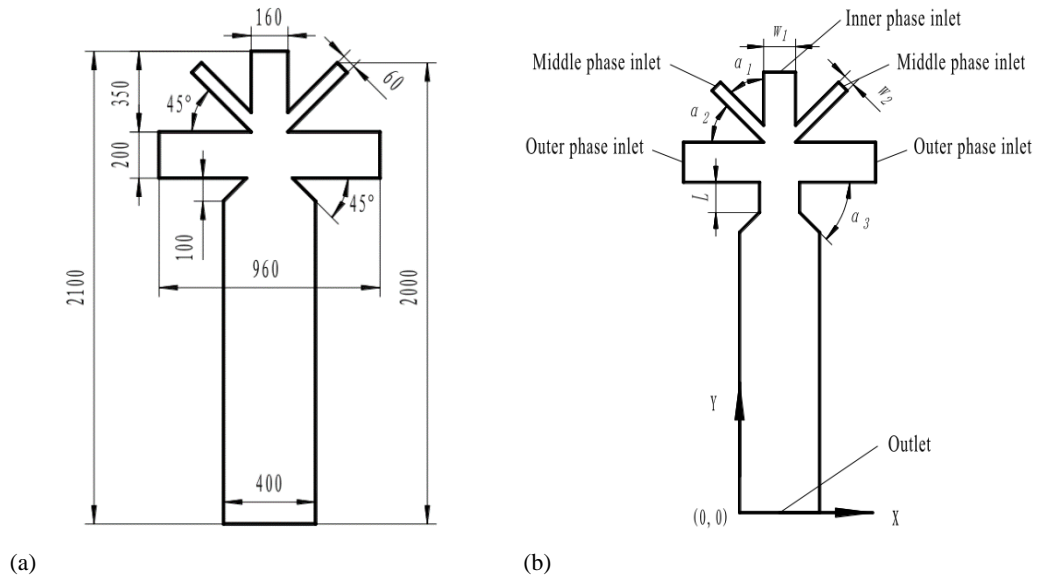
Fig. 1. (a) Initial dimensions. (b) Coordinate system, boundary names, and variable structural parameters.

3.2 Fluid Flow Form and Mechanism Analysis

Fluids in conventional parallel microchannels, e.g., double-T-shaped microchannels and microchannels with combined T-shaped and cross-shaped structures, generally undergo two two-phase flows with mutual shearing and squeezing to prepare double emulsion droplets. In contrast, the six-way junction microchannel in this paper enables the three phases to interact with one another simultaneously.

The force analysis of a droplet is shown in Fig. 2. In the figure, the directions of Q_1, Q_2, and Q_3 are the flow directions of the inter, middle and outer phases, respectively; the direction of out flow is the exit direction of the droplets. Similar to the single emulsion droplet, the double emulsion droplet is subjected to the interaction of the separation force that promotes droplet separation and the retaining force that prevents droplet separation (Wu *et al.* 2015). The interfacial tension F_σ in the direction opposite to the direction of droplet movement prevents the droplet neck from breaking and acting as a retaining force. The linear momentum force F_L caused by the fluid momentum inside the microchip is the separation force that accelerates the breakage of the droplet neck. The Stokes-like force F_S consisting of viscous stress and pressure stress also promotes droplet separation, and the droplet will separate only when the droplet expands to a certain degree. Hence, the Stokes-like force is presumably positively correlated with the droplet radius. In a microfluidic flow at low Reynolds numbers (0.001-0.5), the inertial force is 10^4-10^7 times smaller than other microfluidic forces; therefore, we can ignore the inertial force.

The process of droplet forming is shown in Fig. 3. In the initial state, we fill the inner- and middle-phase channels with the corresponding fluid and the remainder of the microchip with the outer phase, as
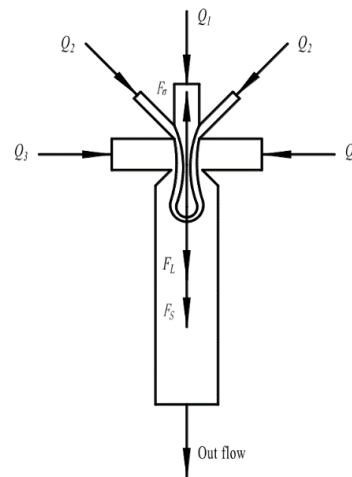
Fig. 2. Force analysis.
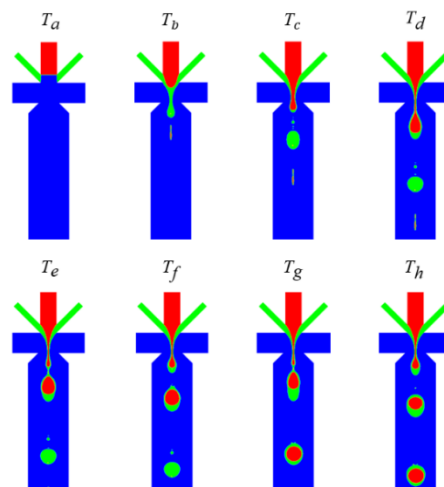
Fig. 3. Droplet forming process.

shown in the T_a state. The middle phase wraps around the inner phase, and the interfacial tension, which is the dominant force, maintains the elongated droplet (Utada *et al.* 2007). The excess middle phase is in the shape of a pendant droplet, as shown in the T_b state. The separation forces, such as linear momentum forces and Stokes-like forces, become more important. When the separation force gradually exceeds the retaining force, the pendant droplet of the middle phase separates and gradually tends to a spherical shape under the action of interfacial tension, as shown in the T_c and T_d states. Similar to the pendant droplet in the middle phase, the first double emulsion droplet is formed, as shown in the T_e and T_f states. The droplets continue to form, as shown in the T_g and T_h states. Microfluidic chips using this new form of fluid flow to prepare double emulsion droplets can reduce the chip area, save cost and improve the droplet production efficiency.

3.3 Numerical Simulation Setup

The software used for numerical simulations in this paper is ANSYS Fluent, and the meshing of the numerical simulation model is performed in the ANSYS Workbench Mesh module. The mesh shape is a quadrilateral, as shown in Fig. 4.
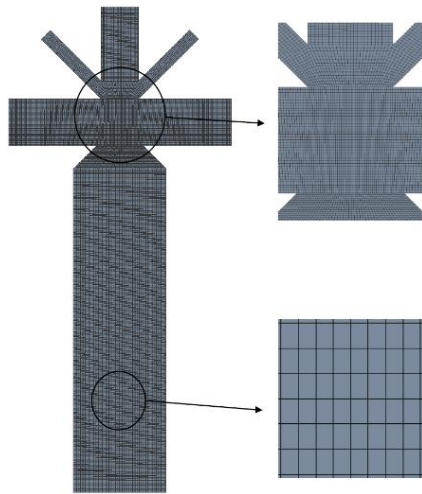
Fig. 4. Model meshing.

In this paper, the laminar flow model is selected for numerical simulations; the VOF model is selected for the multiphase flow model; the pressure-velocity coupling solution algorithm is SIMPLE; the spatial discretization is Least Squares Cell Based gradient difference; the pressure difference is PRESTO; the momentum equation is Second-Order Upwind; the reconstruction between phases interfaces is Geo-Reconstruct (Gueyffier *et al.* 1999). The time step length is set to 2×10^{-5}, and the maximum number of iterations per time step is 120.

3.4 Mesh Independence Analysis

Usually, a larger number of meshes corresponds to more accurate numerical simulation results, but a

longer required computation duration. Therefore, it is especially essential to perform mesh independence analysis to balance the computational error and computation duration. The physical properties and boundary conditions are the interfacial tension $\sigma_{12} = 0.005$ N/m, viscosity $\mu_1 = 0.001$ Pa·s, inner phase flow rate $Q_1 = 48$ ml/min, interfacial tension ratio $\sigma_{12}{:}\sigma_{23} = 1{:}1$, three-phase viscosity ratio $\mu_1{:}\mu_2{:}\mu_3 = 1{:}1{:}5$, and flow rate ratio $Q_1{:}Q_2{:}Q_3 = 40{:}27{:}250$. When the mesh size is 2.5-5 μm, the droplet formation is shown in Fig. 5. The droplet forming results are better and similar when the mesh size is 2.5-3 μm.
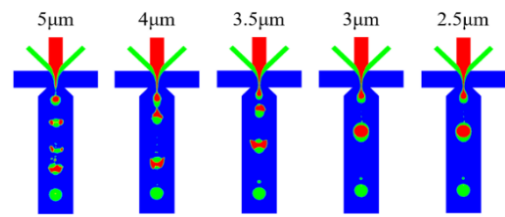
Fig. 5. Droplet formation with different mesh sizes.

When calculating 6000 time steps (120 ms), the relationship between model mesh and calculation duration of numerical simulations is shown in Fig. 6. When the mesh size decreases from 5 μm to 2.5 μm, the number of meshes increases from 27283 to 107831, which is a 3.95-fold increase, and the computation duration increases from 107 minutes to 231 minutes, which is a 2.16-fold increase.
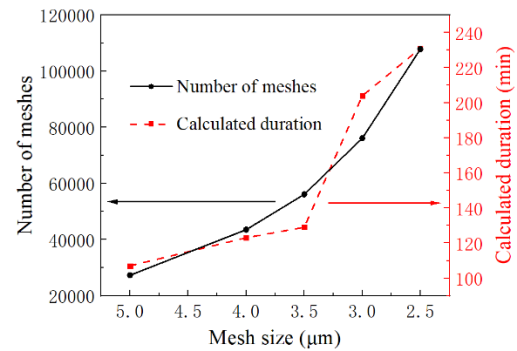
Fig. 6. Relationship between mesh and calculation duration.

To reduce the computational errors and save computational resources, the mesh size of the model numerical simulations is selected as 3 μm.

3.5 Numerical Simulation Feasibility Verification

The initial structure of the microchannels in this paper is similar to that of Deshpande *et al.* (2016). Deshpande S et al. investigated the relationship between the outer- to inner-phase flow velocity ratio and droplet size, where they used water as the inner and outer phases and 1-octanol as the middle phase. In this paper, the structure is modelled and numerically simulated. As shown in Fig. 7, the
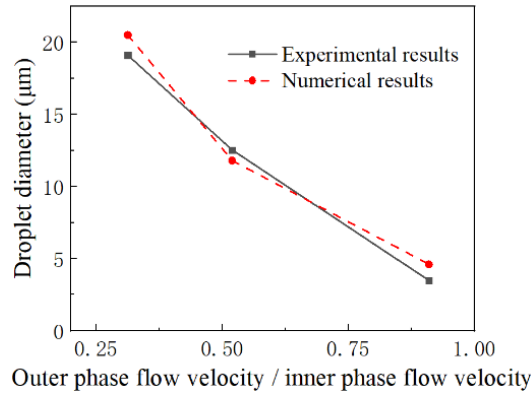
Fig. 7. Comparison of numerical simulation results with experimental results.
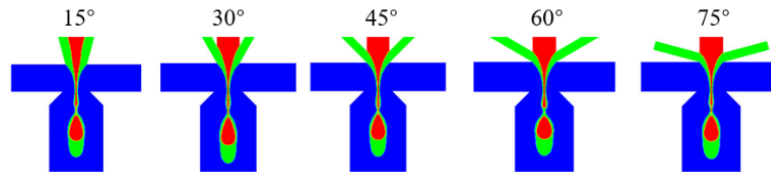
Fig. 8. Volume distribution of forming phases of droplets.

numerical simulation results are similar to the experimental results of Deshpande S et al., which proves the feasibility of the method and setup of the numerical simulation in this paper.

4. RESULTS AND DISCUSSION

4.1 Effect of the Angles Between Inlet Channels on the Droplet Formation

The change in angle between the inlet channels of the three phases changes the force between the continuous and dispersed phases, which affects the droplet formation.

4.1.1 Effect of the Angle Between Inner- and Middle-Phase Channels on the Droplet Formation

This section changes angle α_1 between inner- and middle-phase channels. When the physical properties and boundary conditions are the interfacial tension $\sigma_{12} = 0.005$ N/m , viscosity $\mu_1 = 0.01$ Pa·s , inner phase flow rate $Q_1 = 48$ ml/min , interfacial tension ratio $\sigma_{12}:\sigma_{23} = 1:1$, three-phase viscosity ratio $\mu_1:\mu_2:\mu_3 = 1:1:5$, and flow rate ratio $Q_1:Q_2:Q_3 = 40:27:250$, the double emulsion droplet forming pattern is under the drip flow pattern. The volume distribution of forming phases of the droplets at different α_1 under the drip flow pattern is shown in Fig. 8. A small fluid column similar to a jet section appears inside the microchip. There are breaking positions of the double emulsion droplets at a certain distance from the intersection of the three-phase channels. And the droplet is formed with a similar shape and regularity, but the breaking positions have changed. Assuming that the distance between a

double emulsion droplet breaking point and the microchip intersection is L_1 , Fig. 9 shows the variation of L_1 at different α_1. The increase in α_1 makes the action point of the middle relative inner-phase force move upstream, the linear momentum force generated by the fluid decreases, and the breaking point distance increases from 242 mm to 288 mm. In practice, the microchip length can be adjusted according to different L_1 to reduce the chip area and save cost.
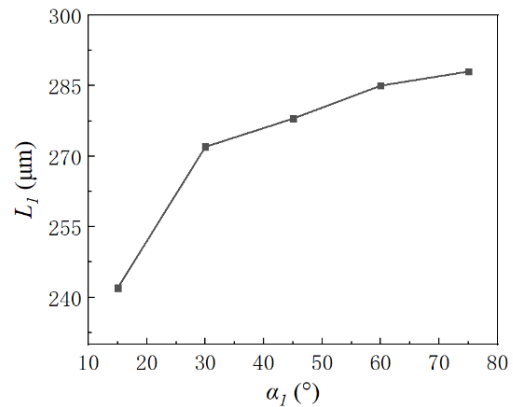
Fig. 9. Variation in L_1 at different α_1.

When $\alpha_1 = 45°$, the microchip produces the first double emulsion droplet at the 0.0434th second. Figure 10 shows the changes in the capillary number and Weber number at the moments before and after the double emulsion droplet breaks. Both capillary number and Weber number increase, which indicates that the dominant role of interfacial tension has decreased and the role of viscous forces has been strengthened.
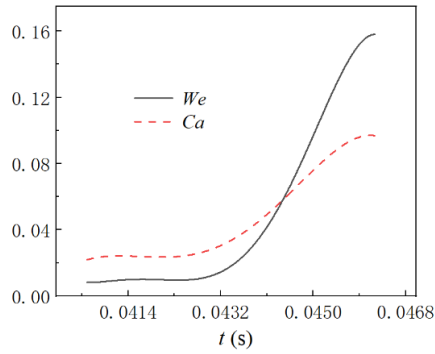
Fig. 10. Variation in the capillary number and Weber number with time.

Figure 11 shows the volume distribution of phases and variation contours of pressure in the moments before and after the double emulsion droplet breakage, respectively. The pressure at the microchip intersection and droplet formation gradually increase before the droplet breakage, and the separation force represented by pressure to promote the droplet separation is strengthened at this time. The pressure is released after the droplet breakage.

Figures 12. (a) and (b) show the distribution curves of velocity and pressure on the symmetry axis of the microchip when the droplet is about to break respectively. Local high velocity and high pressure appear near the droplet breaking point. Therefore, the geometry must be improved during the manufacture
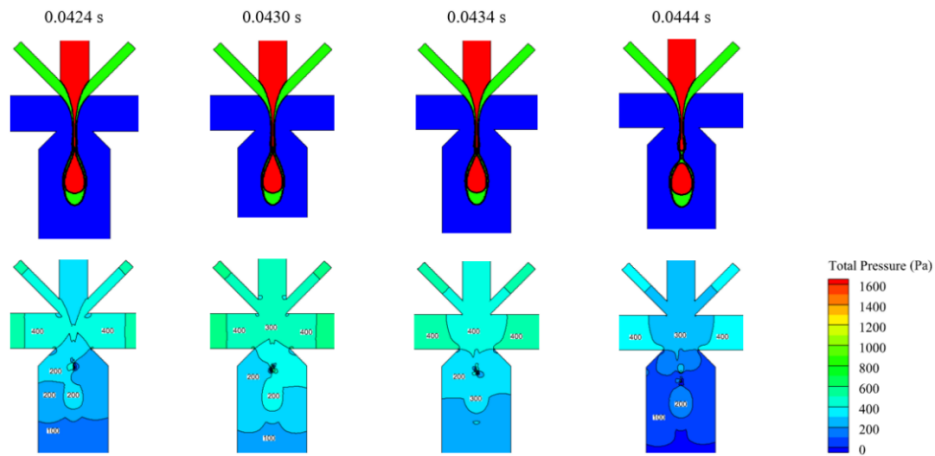
Fig. 11. Volume distribution of phases and variation contours of pressure.

(a)

(b)
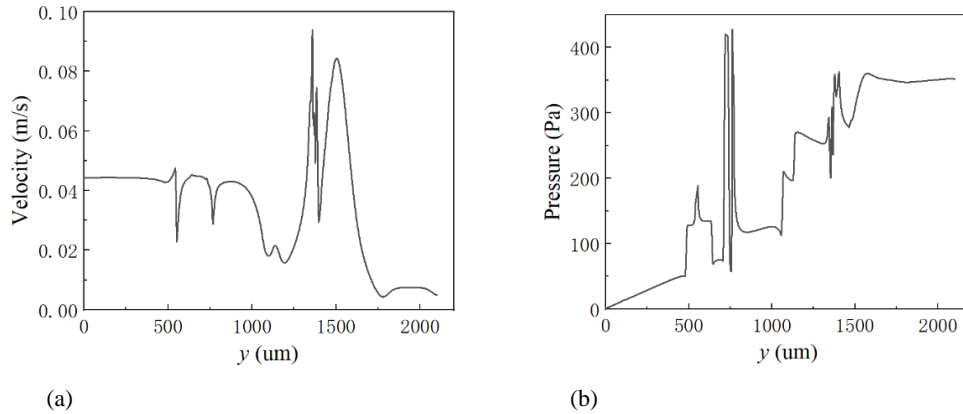
Fig. 12. (a) Distribution curve of velocity. (b) Distribution curve of pressure.

of the microchip to release the internal pressure and avoid damage to the microchip.

Figure 13 shows the volume distribution of forming phases and variation curve of the double emulsion droplet area at different α_1. From the general trend, the area of both outer and inner droplets S_o and S_i decreases due to the increase in squeezing pressure on the inner phase, and all area variations are within 11%; S_1 and S_2 are 2.27 and 2.37, respectively.

As shown in Fig. 13, the area of the inner droplets and angle α_1 roughly show a second-order nonlinear relationship. We use a second-order polynomial fit to obtain a functional expression that represents their relationship, as shown in Eq. (9). The area of the outer droplets and angle α_1 roughly show a linear relationship. We use a linear equation fit to obtain a functional expression that represents their relationship, as shown in Eq. (10).

$$S_i = 12995.4 + 14.99\alpha_I - 0.46\alpha_I^2 \qquad (9)$$

$$S_o = 32016.1 - 59.63\alpha_I \qquad (10)$$

The physical properties and boundary conditions were changed to the interfacial tension $\sigma_{12} = 0.005$ N/m , viscosity $\mu_I = 0.1$ Pa·s , inner phase flow rate $Q_I = 640$ mm^3/s, interfacial tension ratio $\sigma_{12}{:}\sigma_{23} = 1{:}1$, three-phase viscosity ratio $\mu_I{:}\mu_2{:}\mu_3 = 10{:}1{:}5$, and flow rate ratio $Q_I{:}Q_2{:}Q_3 = 32{:}27{:}200$. The double emulsion droplet forming pattern was converted to a jet flow pattern.
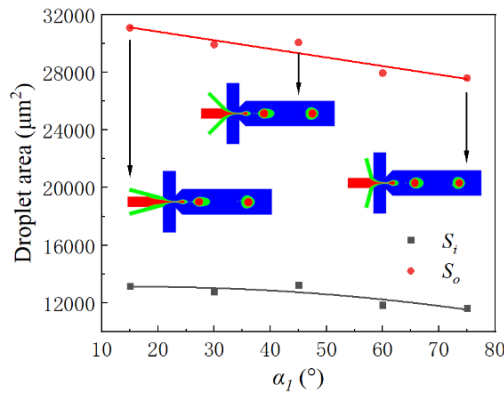
Fig. 13. Effect of different α_I on the droplet forming area and forming process under the drip flow pattern.
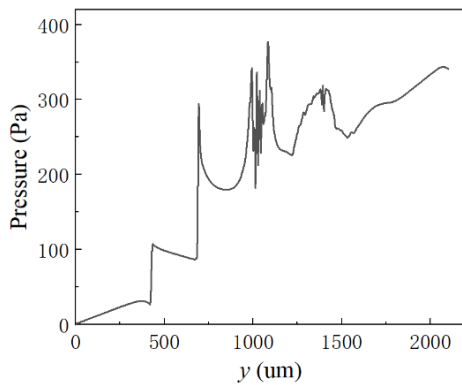
Fig. 14. Distribution curve of pressure.

Figure 14 shows the distribution curve of pressure on the symmetry axis of the microchip when a droplet is about to break. The maximum pressure under the jet flow pattern is smaller than that under the drip flow pattern. The pressure under the drip flow pattern is concentrated upstream of the chip, while the pressure under the jet flow pattern is concentrated in the middle and upstream. In actual production, the jet flow pattern can be used to produce microdroplets to facilitate the dispersion distribution of pressure.

Figure 15 shows the volume distribution of forming phases and variation curves of the droplet area. Similar to the case of drip flow, the droplets breaking

positions of the jet flow pattern do not vary much from the distance of the microchip intersection, and the area of the inner and outer droplets decreases. The change in droplet area under the jet flow pattern is smaller than that of the drip flow pattern (both within 5%). S_I and S_2 are 2.60 and 2.71, respectively. The effect of α_I on the relative wall thickness is small.
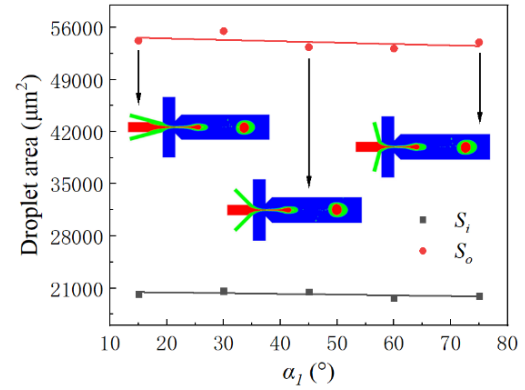
Fig. 15. Effect of different α_I on the forming area and forming process of droplets under the jet flow pattern.

The areas of the inner and outer droplets are approximately linearly related to angle α_I as shown by linear equation fitting using Eqs. (11) and (12), respectively.

$$S_i = 20630.6 - 9.91\alpha_I \qquad (11)$$

$$S_o = 54892.9 - 18.65\alpha_I \qquad (12)$$

CV_i and CV_o are shown in Fig. 16. CV_i is 2.42-4.41%, CV_o is 2.07-3.15% under the drip flow pattern, and *C.V.* satisfies the requirements of industrial production (less than 5%). When α_I is 60°, the monodispersity of the inner and outer droplet areas is optimal. In the jet flow pattern, CV_i is 1.00-5.79%, and CV_o is 0.64-4.94%. When α_I is 60°, the monodispersity of the inner and outer droplet areas is optimal.

4.1.2 Effect of the Angle Between Middle- and Outer-Phase Channels on the Droplet Formation

The volume distribution of forming phases and variation curve of the forming droplet area at different α_2 values under the drip flow pattern are shown in Fig. 17. (a) The physical properties and boundary conditions are the interfacial tension $\sigma_{12} = 0.005$ N/m , viscosity $\mu_I = 0.004$ Pa·s , inner phase flow rate $Q_I = 48$ ml/min, interfacial tension ratio $\sigma_{12}{:}\sigma_{23} = 1{:}1$, three-phase viscosity ratio $\mu_I{:}\mu_2{:}\mu_3 = 4{:}4{:}5$, and flow rate ratio $Q_I{:}Q_2{:}Q_3 = 40{:}27{:}250$. When α_2 increases from 15° to 75°, the areas of both inner and outer droplets first increase and subsequently decrease, and the area of
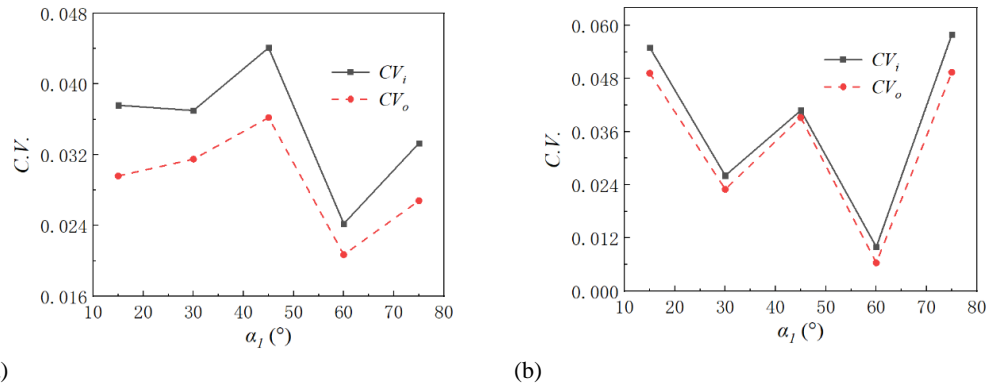
(a)   (b)

Fig. 16. (a) Effect of α_1 on the monodispersity of droplet areas under the drip flow pattern. (b) Effect of α_1 on the monodispersity of droplet areas under the jet flow pattern.

(a)   (b)
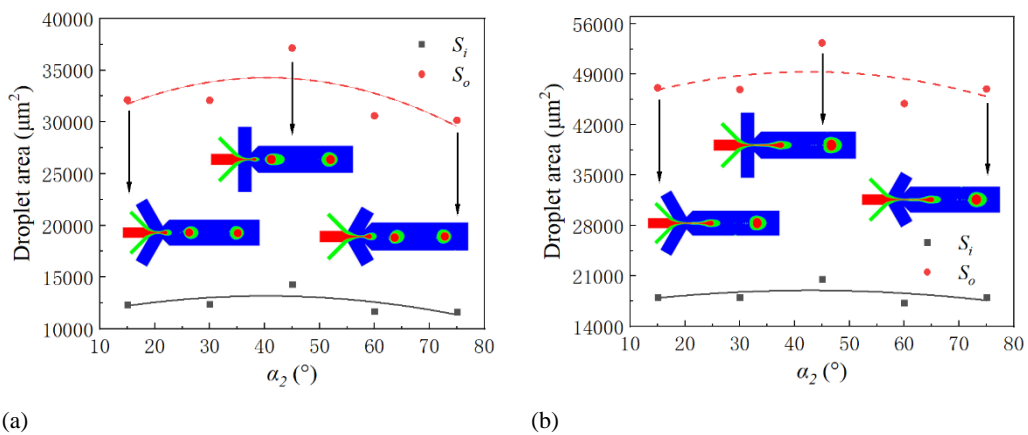
Fig. 17. (a) Effect of different α_2 on the forming droplet area and forming process under the drip flow pattern. (b) Effect of different α_2 on the forming droplet area and forming process under the jet flow pattern.

the droplets is maximal when α_2 is 45°. The breaking points of the droplets are near the expansion angle. When α_2 increases from 15° to 45°, the position of the inner and middle phases by the force of the outer phase is constantly moving upstream, and the effective force near the breaking point is decreasing. The fluid column of parallel-like flow can continuously stretch, and the position of the breaking point is constantly moving downstream; the filling time of the inner and middle phases increases. Therefore, in this angular interval, the inner and outer droplet areas will have some growth. When α_2 increases from 15° to 45°, the velocity components of the three phases along the symmetry axis direction are in the same direction. When α_2 increases from 45° to 75°, at the intersection of the three phases, the direction of the velocity component of the outer phase along the symmetry axis of the microchip is changed, and the opposite velocity component has a certain inhibitory effect on the extension of the fluid column. However, this inhibitory effect is not obvious from the change in forming droplet area. From the general trend, during the increase in α_2 from 15° to 75°, the maximum variations in the inner and outer droplet areas are 22.26% and 21.40%, respectively; S_1 and S_2 are 2.59 and 2.62,

respectively, and the area ratios slightly change more than α_1. The change in forming area of the droplets at different α_2 values under the jet flow pattern is shown in Fig. 17. (b) For the jet flow pattern, the interfacial tension is $\sigma_{12} = 0.005$ N/m, the viscosity is $\mu_1 = 0.1$ Pa·s , the inner phase flow rate is $Q_1 = 38.4$ ml/min , the interfacial tension ratio is $\sigma_{12}:\sigma_{23} = 1:1$, the viscosity ratio of the three phases is $\mu_1:\mu_2:\mu_3 = 10:1:5$, the flow rate ratio is $Q_1:Q_2:Q_3 = 32:27:200$, and the variation in the droplet area at different α_2 value is not much different from that of the drip flow pattern

Using a second-order polynomial fitting, we obtain a functional expression that represents the droplet area versus angle α_2 under the drip flow pattern, as shown in Eqs. (13) and (14), respectively.

$$S_i = 10759.8 + 120.63\alpha_2 - 1.5\alpha_2^2 \qquad (13)$$

$$S_o = 27860 + 317.91\alpha_2 - 3.93\alpha_2^2 \qquad (14)$$

The functional expressions that represent the relationship between droplet area and angle α_2 under the jet flow pattern are shown in Eqs. (15) and (16), respectively.

$$S_i = 16528.2 + 115.23\alpha_2 - 1.13\alpha_2^2 \qquad (15)$$

$$S_o = 43376 + 279.97\alpha_2 - 3.28\alpha_2^2 \qquad (16)$$

CV_i and CV_o are shown in Fig. 18. CV_i is 0.37-3.71%, and CV_o is 1.06-4.36% under the drip flow pattern. When α_2 is 15°, CV_i is optimal; when α_2 is 75°, CV_o is optimal. In the jet flow pattern, CV_i and CV_o are worse than those in the drip flow pattern. The CV_i is 5.68-12.06%, and CV_o is 1.28-8.26%. When α_2 is 45°, CV_i is optimal; when α_2 is 60°, CV_o is optimal.

4.2 Effect of the Width Ratio of the Inner- to Middle-Phase Channel on Droplet Formation

When the width ratio of the inner- to middle-phase channel w_1/w_2 is relatively large, it is possible but more difficult to form thin-walled double emulsion droplets; the width ratio is small and the forming difficulty is low, but the wall thickness is large. In this section, the effect of forming double emulsion droplets with different width ratios is investigated by fixing the width of the inner-phase channel and changing the width of the middle-phase channel.
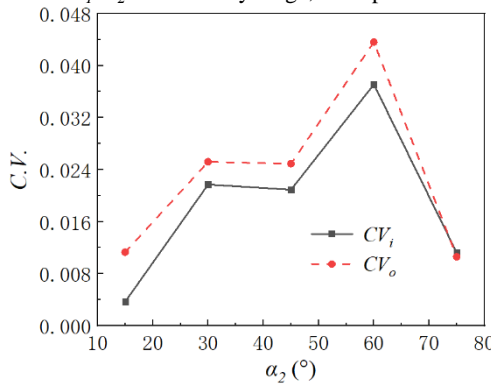
The volume distribution of forming phases and variation curves of the forming droplet area at different width ratios under the drip flow pattern are shown in Fig. 19. (a). The physical properties and boundary conditions are: interfacial tension $\sigma_{12} = 0.002 \text{ N/m}$, viscosity $\mu_1 = 0.04 \text{ Pa·s}$, inner phase flow rate $Q_1 = 38.4$ ml/min, interfacial tension ratio $\sigma_{12}:\sigma_{23} = 1:1$, three-phase viscosity ratio $\mu_1:\mu_2:\mu_3 = 4:4:5$, and flow rate ratio
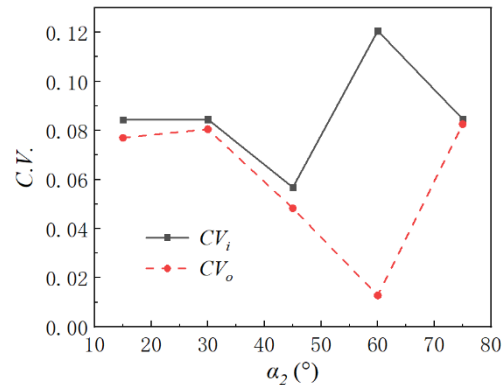
(a)   (b)

Fig. 18. (a) Effect of α_2 on the monodispersity of droplet areas under the drip flow pattern. (b) Effect of α_2 on the monodispersity of droplet areas under the jet flow pattern.

$Q_1:Q_2:Q_3 = 32:27:200$. Under this working condition, the double emulsion droplet formation is stricter for w_2, and can only stably occur when $w_1/w_2 \in (2.7,4)$. In terms of the general trend, when w_1/w_2 increases from 2.7 to 4, the area of the outer droplets decreases by 6.53%, while the area of the inner droplets increases by of 20.74%. S_1 and S_2 are 2.14 and 2.68, respectively, which shows that the width ratio has a greater effect on the area of the inner droplets and the relative wall thickness of the double emulsion droplets. The smaller w_2 corresponds to less middle phase that can be used to wrap the inner phase, a smaller viscous force on the inner phase, and a delay time point of inner droplet breakage, so the area of the inner droplet will continue growing. The decrease in w_2 decreases the middle phase, so the area of the outer droplets will gradually decrease.

Unlike the drip flow pattern, the jet flow pattern has lower requirements for w_2. However, when w_2 is too large, 2-3 inner droplets wrapped in one outer droplet can occur. In this section, only the case where a single droplet is wrapped is discussed. Figure 19. (b) shows the effect of different width ratios of channels on the droplet formation under the jet flow pattern.

The physical properties and boundary conditions are: interfacial tension $\sigma_{12} = 0.005 \text{ N/m}$, viscosity $\mu_1 = 0.1 \text{ Pa·s}$, inner phase flow rate $Q_1 = 38.4$ ml/min, interfacial tension ratio $\sigma_{12}:\sigma_{23} = 1:1$, three-phase viscosity ratio $\mu_1:\mu_2:\mu_3 = 10:1:5$, and flow rate ratio $Q_1:Q_2:Q_3 = 32:27:200$. The trend of the inner and outer droplet areas under the jet flow pattern is consistent with that under the drip flow pattern. In the process of decreasing w_2, the squeezing pressure on the inner phase decreases, the necked section formed by the inner phase widens, and the pressure decreases. Therefore, the breakage of the inner droplets will be continuously delayed, and their area will be continuously increased. When w_2 decreases, the flow rate of the middle phase decreases, so the area of the outer droplets decreases. The change in the width ratio of channels has less effect on the size of the forming droplet area under the jet flow pattern than under the drip flow pattern. In general, the inner droplet area increases by 6.14% and the outer droplets area decreases by 15.86% when w_1/w_2 increases from 2.7 to 4. S_1 and S_2 are 2.14 and 2.70, respectively. In summary, changing the width ratio of the channel is more effective in regulating the ratio

(a)

(b)
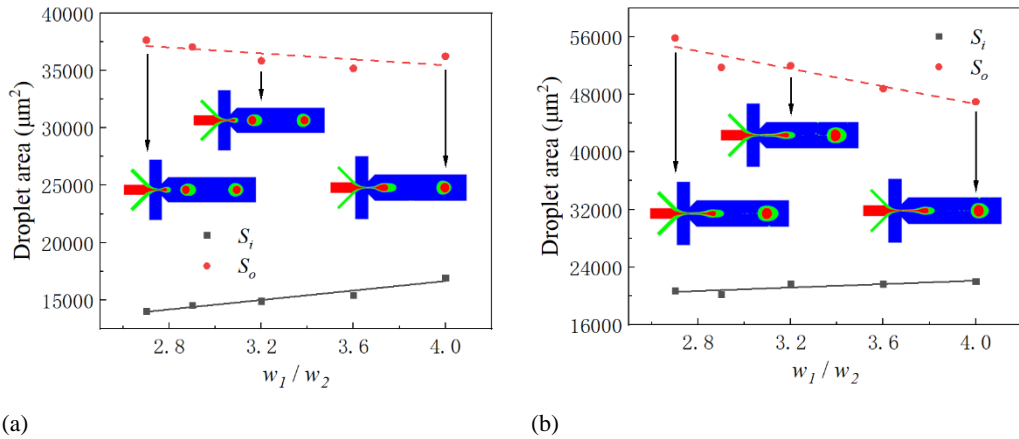
Fig. 19. (a) Effect of different width ratios of channels on the forming droplet area and process under the drip flow pattern. (b) Effect of different width ratios of channels on the forming droplet area and process under the jet flow pattern.

(a)

(b)
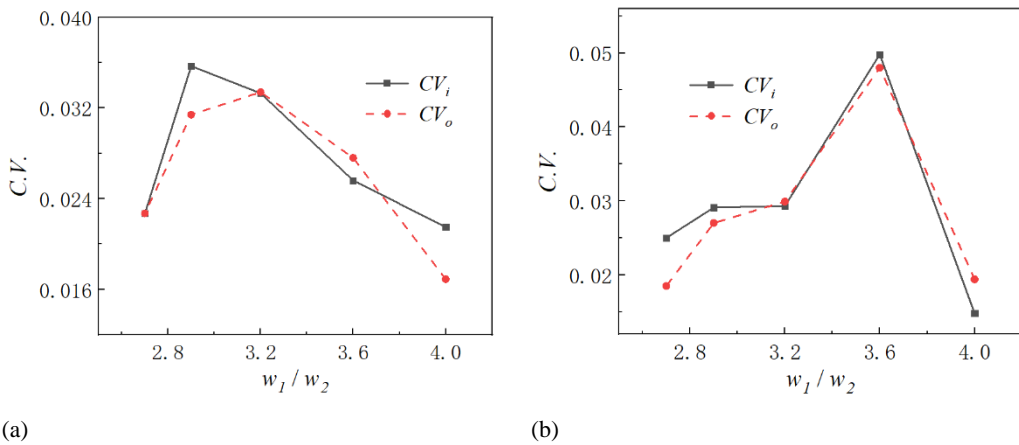
Fig. 20. (a) Effect of the width ratio of channels on the monodispersity of the droplet area under the drip flow pattern. (b) Effect of the width ratio of channels on the monodispersity of the droplet area under the jet flow pattern.

of the droplet area than changing the channel angles. It can better adjust the relative wall thickness of the double emulsion droplet.

Linear equation fitting is used to obtain a functional expression of the relationship between droplet area and width ratio of channels w_1/w_2 under the drip flow pattern, as shown in Eqs. (17) and (18), respectively.

$$S_i = 8418.47 + 2058.39w_1/w_2 \tag{17}$$

$$S_o = 40634.05 - 1294.22w_1/w_2 \tag{18}$$

The functional expressions of the relationship between droplet area and width ratio of channels w_1/w_2 under the jet flow pattern are shown in Eqs. (19) and (20), respectively.

$$S_i = 17347.02 + 1192.31w_1/w_2 \tag{19}$$

$$S_o = 71121.62 - 6111.71w_1/w_2 \tag{20}$$

CV_i and CV_o are shown in Fig. 20. CV_i is 2.15-3.57%, and CV_o is 1.69-3.34% under the drip flow pattern. When w_1/w_2 is 4, the monodispersity of the

inner and outer droplet areas is optimal. In the jet flow pattern, CV_i is 1.48-4.98%, and CV_o is 1.85-4.80%. When w_1/w_2 is 4, the monodispersity of the inner droplet area is optimal; when w_1/w_2 is 2.7, the monodispersity of the outer droplet area is optimal.

4.3 Effect of the Expansion Angle on the Droplet Formation

In preparing microdroplets using cross-shaped flow-focusing structures, the force between continuous and dispersed phases can be enhanced by using a focusing hole, expansion angle, or a combination of both.

4.3.1 Effect of the Length of the Focusing Hole on Droplet Formation

The physical properties and boundary conditions are: interfacial tension $\sigma_{12} = 0.0015$ N/m , viscosity $\mu_1 = 0.004$ Pa·s , inner phase flow rate $Q_1 = 48$ ml/min , interfacial tension ratio $\sigma_{12}:\sigma_{23} = 1:1$, three-phase viscosity ratio
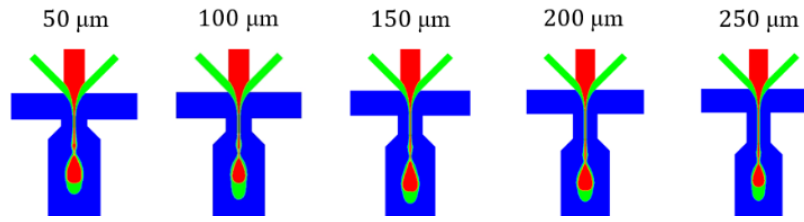
Fig. 21. Volume distribution of forming phases of droplets.
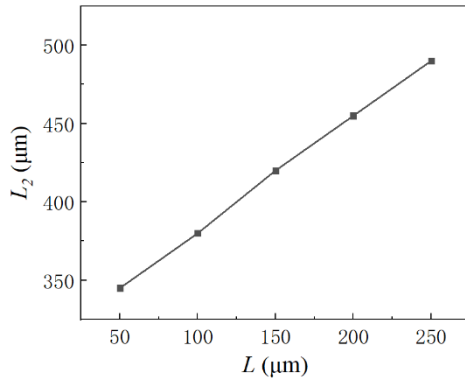
Fig. 22. Variation of L_2 at different L.

$\mu_1 : \mu_2 : \mu_3 = 4:4:15$, and flow rate ratio $Q_1 : Q_2 : Q_3 = 40:27:250$. The volume distribution of forming phases of droplets in microchips with different lengths of the focusing hole is shown in Fig. 21. When the length of the focusing hole increases, the length of the jet section increases and the breaking position keeps moving downstream. Assuming that the distance between the breaking position of the droplets and the microchip intersection is L_2, Fig. 22 shows the variation in L_2 under different lengths L of the focusing hole, which shows that the moving distance of the breaking position is close to the increase in length of the focusing hole.

The volume distribution of forming phases and variation curves of the droplet area are given in Fig. 23. In terms of the general trend, the variation in length L of the focusing hole does not greatly influence the forming droplet area, and its main effect is reflected in the elongation of the jet section. The jet section only makes the droplets pass through a longer acceleration section, but because the structure downstream of the focusing hole does not change, the fluid motion in the microchip is not fundamentally different, so there is no significant variation in the droplet area. The maximum variation of the area of both the inner and outer droplets do not exceed 10%; S_1 and S_2 are 2.28 and 2.36, respectively.

Using a second-order polynomial fitting, a functional expression for the relationship between droplet area and focusing hole length L can be obtained, as shown in Eqs. (21) and (22), respectively.

$$S_i = 13556.8 - 7.37L + 0.03L^2 \tag{21}$$

$$S_o = 30928.4 - 10.3L - 0.04L^2 \tag{22}$$

CV_i and CV_o are shown in Fig. 24. CV_i is 3.53-6.05%, and CV_o is 3.70-5.71% under the drip flow pattern. When L is 50 μm, the monodispersity of the inner and outer droplet areas is optimal. When L increases to 200 μm, CV_i and CV_o are high, and it is
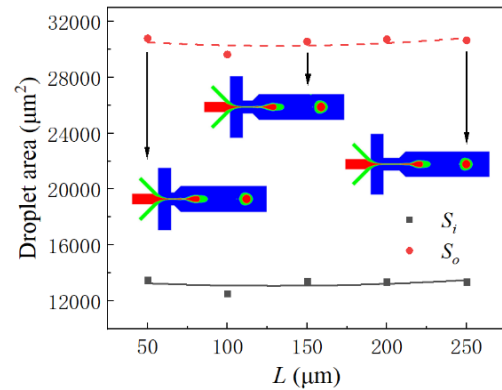
Fig. 23. Effect of microchips with different lengths of the focusing hole on the forming droplet area and forming process.
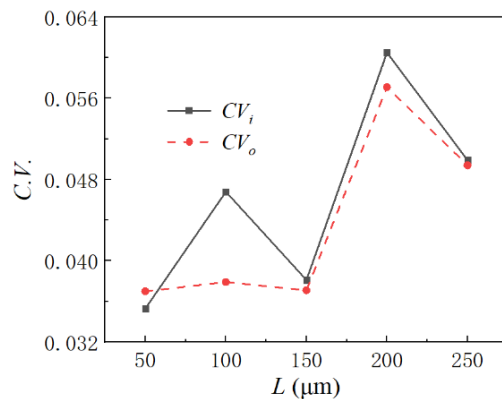
Fig. 24. Effect of the length of the focusing hole on the monodispersity of the droplet area.

difficult to satisfy the actual production requirements. Therefore, attention must be paid to shortening the length of the focusing hole when designing the channel.

4.3.2 Effect of the Expansion Angle on the Droplet Formation

Figure 25 shows the volume distribution of forming phases and variation curves of the droplet area under different α_3. The physical properties and boundary conditions are: interfacial tension $\sigma_{12} = 0.005$ N/m, viscosity $\mu_1 = 0.004$ Pa·s , inner phase flow rate $Q_1 = 48$ ml/min , interfacial tension ratio $\sigma_{12}:\sigma_{23} = 1:1$, three-phase viscosity ratio $\mu_1:\mu_2:\mu_3 = 4:4:15$, and flow rate ratio $Q_1:Q_2:Q_3 = 40:27:250$. Changing the expansion angle does not affect the flow pattern in this working condition, and the flow pattern is a drip flow pattern in all structures. When α_3 increases from 15° to 75°, the general trend shows that the area of the inner droplets decreases by 29.10% and the area of the outer droplets decreases by 29.24%. S_1 and S_2 are 2.28 and 2.29, respectively, which show that the change in expansion angle has a greater effect on the adjustment of the droplet area and a smaller effect on the adjustment of the relative wall thickness of the droplets.
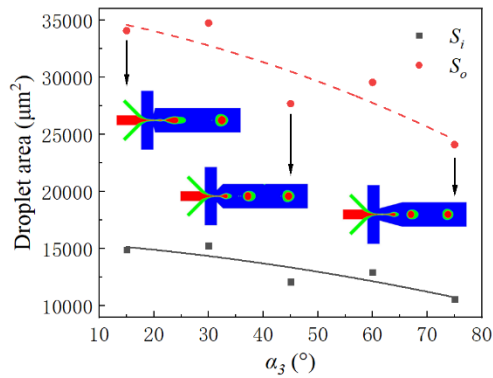
Fig. 25. Effect of microchips with different expansion angles on the forming droplet area and forming process.

Using a second-order polynomial fitting, we obtain a functional expression that represents the relationship between droplet area and angle α_3, as shown in Eqs. (23) and (24), respectively.

$$S_i = 15734 - 32.35\alpha_3 - 0.46\alpha_3^2 \tag{23}$$

$$S_o = 35893 - 72.49\alpha_3 - 1.05\alpha_3^2 \tag{24}$$

CV_i and CV_o are shown in Fig. 26. CV_i is 3.15-5.4%, and CV_o is 3.41-5.43%. When α_3 is 45°, the monodispersity of the inner droplet area is optimal; when α_3 is 75°, the monodispersity of the outer droplet area is optimal.

5. CONCLUSION

In this paper, a simplified double-cross-shaped microchannel is numerically simulated using the VOF method to investigate the forming process and quality of double emulsion droplets under different
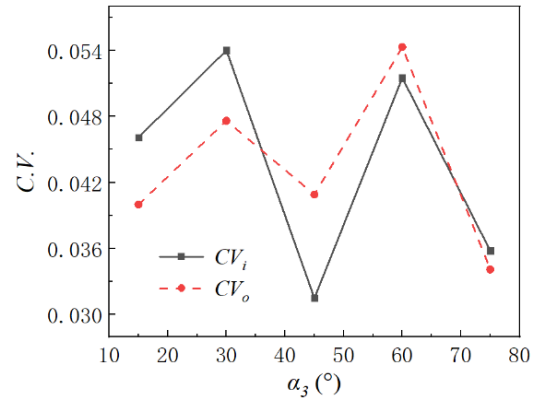
Fig. 26. Effect of the expansion angle on the monodispersity of the droplet area.

microchannel geometric parameters. The results are summarized as follows.

(1) The increase in the angle between the inner and middle phases decreases the area of both inner and outer droplets of the double emulsion droplets, while the increase in the angle between the middle and outer phases first increases and subsequently decreases the inner and outer droplet areas of the double emulsion droplets.

(2) The increase in width ratio of the inner- to middle-phase channel increases the inner droplet area, decreases the outer droplet area of the double emulsion droplets, and decreases the relative wall thickness of the double emulsion droplets.

(3) The change in length of the focusing hole can change the forming flow pattern of double emulsion droplets. A greater focusing hole length corresponds to a greater length of the jet section, but the change in the area of the forming double emulsion droplet is smaller. The increase in expansion angle can decrease the forming area of the double emulsion droplets and has a greater effect on the adjustment of the droplet area.

(4) In terms of monodispersity, the coefficient of variation of the double emulsion droplet area with different geometries under the drip flow pattern are within 5%, which can satisfy the actual production requirements. Nevertheless, there are certain fluctuations in the coefficient of variation under the jet flow pattern, which cannot be applied to occasions with high requirements of monodispersity at present.

(5) The geometric parameters were curve-fitted to the droplet area, and a functional expression of their relationship was obtained.

REFERENCES

Deshpande, S. and C. Dekker (2018). On-chip microfluidic production of cell-sized liposomes. *Nature Protocols* 13(5), 856-874.

Deshpande, S., Y. Caspi, A. E. Meijering and Dekker, C. (2016). Octanol-assisted liposome assembly on chip. *Nature Communications* 7(1), 1-9.

Fani, M., P. Pourafshary, P. Mostaghimi and N. Mosavat (2022). Application of microfluidics in chemical enhanced oil recovery: A review. *Fuel* 315, 123225.

Gueyffier, D., J. Li, A. Nadim, R. Scardovelli and S. Zaleski (1999). Volume-of-fluid interface tracking with smoothed surface stress methods for three-dimensional flows. *Journal of Computational Physics* 152(2), 423-456.

Han, W. and X. Chen (2021). A review on microdroplet generation in microfluidics. *Journal of the Brazilian Society of Mechanical Sciences and Engineering* 43(5), 1-12.

He, S., N. Joseph, S. Feng, M. Jellicoe and C. L. Raston (2020). Application of microfluidic technology in food processing. *Food and Function* 11(7), 5726-5737.

Hidema, R., R. Ohashi, S. J. Muller and H. Suzuki (2021). Effects of channel geometry and physicochemical properties of solutions on stable double emulsion production in planar microfluidic devices having triangular orifices. *AIP Advances* 11(6), 065219.

Illath, K., S. Kar, P. Gupta, A. Shinde, S. Wankhar, F. G. Tseng and T. S. Santra (2021). Microfluidic nanomaterials: From synthesis to biomedical applications. *Biomaterials* 121247.

Jiang, F., Y. Xu, J. Song and H. Lu (2019). Numerical study on the effect of temperature on droplet formation inside the microfluidic chip. *Journal of Applied Fluid Mechanics* 12(3), 831-843.

Kanouni, M., H. L. Rosano and N. Naouli (2002). Preparation of a stable double emulsion (W1/O/W2): role of the interfacial films on the stability of the system. *Advances in Colloid and Interface Science* 99(3), 229-254.

Ko, D. H., A. Hosseini, H. Karaosmanoglu, K. Taredun, L. Jones and A. Partridge (2022). Microfluidic separation of capture from detection and its application for determination of COVID-19 antibodies. *Sensors and Actuators B: Chemical* 351, 130918.

Lian, J., X. Luo, X. Huang, Y. Wang, Z. Xu and X. Ruan (2019). Investigation of microfluidic co-flow effects on step emulsification: Interfacial tension and flow velocities. *Colloids and Surfaces A: Physicochemical and Engineering Aspects* 568, 381-390.

Liu, Z., M. Chai, X. Chen, S. H. Hejazi and Y. Li (2021). Emulsification in a microfluidic flow-focusing device: Effect of the dispersed phase viscosity. *Fuel* 283, 119229.

Liu, Z., J. Zhao, Y. Pang and X. Wang (2018). Generation of droplets in the T-junction with a constriction microchannel. *Microfluidics and Nanofluidics* 22(11), 1-9.

Muhsin, S. A., M. Al-Amidie, Z. Shen, Z. Mlaji, J. Liu, A. Abdullah and M. Almasri (2022). A microfluidic biosensor for rapid simultaneous detection of waterborne pathogens. *Biosensors and Bioelectronics* 113993.

Nabavi, S. A., G. T. Vladisavljević, S. Gu and E. E. Ekanem (2015). Double emulsion production in glass capillary microfluidic device: Parametric investigation of droplet generation behaviour. *Chemical Engineering Science* 130, 183-196.

Sapei, L., M. A. Naqvi and D. Rousseau (2012). Stability and release properties of double emulsions for food applications. *Food hydrocolloids* 27(2), 316-323.

Sartipzadeh, O., S. M. Naghib, A. Seyfoori, M. Rahmanian and F. S. Fateminia (2020). Controllable size and form of droplets in microfluidic-assisted devices: Effects of channel geometry and fluid velocity on droplet size. *Materials Science and Engineering: C* 109, 110606.

Schaich, M., D. Sobota, H. Sleath, J. Cama and U. F. Keyser (2020). Characterization of lipid composition and diffusivity in OLA generated vesicles. *Biochimica et Biophysica Acta (BBA)-Biomembranes* 1862(9), 183359.

Schmidt-Speicher, L. M., and K. Länge (2021). Microfluidic integration for electrochemical biosensor applications. *Current Opinion in Electrochemistry* 29, 100755.

Shao, C., J. Chi, L. Shang, Q. Fan and F. Ye (2021). Droplet microfluidics-based biomedical microcarriers. *Acta Biomaterialia*.

Shi, Y., Y. Cai, Y. Cao, Z. Hong and Y. Chai (2021). Recent advances in microfluidic technology and applications for anti-cancer drug screening. *TrAC Trends in Analytical Chemistry* 134, 116118.

Souza, L. and A. Al-Tabbaa (2018). Microfluidic fabrication of microcapsules tailored for self-healing in cementitious materials. *Construction and Building Materials* 184, 713-722.

Stauffer, F., B. Peter, H. Alem, D. Funfschilling, N. Dumas, C. A. Serra and T. Roques-Carmes (2019). Polyelectrolytes layer-by-layer surface modification of PDMS microchips for the production of simple O/W and double W/O/W emulsions: From global to localized treatment. *Chemical Engineering and Processing-Process Intensification* 146, 107685.

Su, W., D. Liang and M. Tan (2021). Microfluidic strategies for sample separation and rapid

detection of food allergens. *Trends in Food Science and Technology* 110, 213-225.

Tan, S., C. Gao, H. Liu, B. Ye and D. Sun (2020). Research of double emulsion formation and shell-thickness influence factors in a novel six-way junction microfluidic device. *Colloids and Surfaces A: Physicochemical and Engineering Aspects* 601, 124917.

Tivony, R., M. Fletcher, K. Al Nahas and U. F. Keyser (2021). A microfluidic platform for sequential assembly and separation of synthetic cell models. *ACS Synthetic Biology* 10(11), 3105-3116.

Utada, A. S., A. Fernandez-Nieves, H. A. Stone and D. A. Weitz (2007). Dripping to jetting transitions in coflowing liquid streams. *Physical Review Letters* 99(9), 094502.

Vaezi, Z., M. Sedghi, M. Ghorbani, S. Shojaeilangari, A. Allahverdi and H. Naderi-Manesh (2020). Investigation of the programmed cell death by encapsulated cytoskeleton drug liposomes using a microfluidic platform. *Microfluidics and Nanofluidics* 24(7), 1-15.

Wu, P., Z. Luo, Z. Liu, Z. Li, C. Chen, L. Feng and L. He (2015). Drag-induced breakup mechanism for droplet generation in dripping within flow focusing microfluidics. *Chinese Journal of Chemical Engineering* 23(1), 7-14.

Xing, G., W. Zhang, N. Li, Q. Pu and J. M. Lin (2021). Recent progress on microfluidic biosensors for rapid detection of pathogenic bacteria. *Chinese Chemical Letters*.

Zhang, C., W. Gao, Y. Zhao and Y. Chen (2018). Microfluidic generation of self-contained multicomponent microcapsules for self-healing materials. *Applied Physics Letters* 113(20), 203702.

Zhao-Miao, L. I. U., D. U. Yu and P. A. N. G. Yan (2018). Generation of water-in-oil-in-water (W/O/W) double emulsions by microfluidics. *Chinese Journal of Analytical Chemistry* 46(3), 324-330.